AIAA-2008-7326

26th AIAA Applied Aerodynamics Conference

Proximity Aerodynamics Analyses for Launch Abort Systems

William Chan*, Goetz Klopfer†, Jeffrey Onufer‡, Shishir Pandya§

NASA Ames Research Center, M/S T-27B, Moffett Field, CA 94035

Analyses of drag variation with vehicle proximity are performed for two different launch abort systems for NASA's Crew Launch Vehicle: a scaled-up Apollo tractor concept and a side-mounted rockets concept. The results are used to assess the abort capabilities of new crew escape systems. With the complex flow physics involved in the separation of the escape vehicle from the Service Module, both inviscid and viscous simulation methods, under nozzle thrust-on and thrust-off conditions, are evaluated for their ability to predict the axial forces during an ascent abort scenario. Also, the predictive capability of time-accurate simulations involving prescribed and coupled six-degrees-of-freedom motion are investigated in this study. Comparisons are made with wind tunnel data from the Apollo program.

Nomenclature

α	Angle of attack
Δx	Separation distance
Δz	Normal offset distance
D	Capsule diameter
$\frac{\Delta x}{D}$	Non-dimensional axial separation distance
$\frac{\Delta z}{D}$	Non-dimensional normal offset distance
C_A	Axial-force coefficient
y^+	Dimensionless wall distance
M	Freestream or abort Mach number
ΔM	Mach number increment
$\bar{P}$	Dimensional pressure
$\bar{P}_\infty$	Dimensional ambient pressure
P	Non-dimensional pressure
γ	Ratio of specific heats

I. Introduction

The planning of the next generation of NASA's launch capability to low earth orbit, Moon, and Mars is underway. The proposed Crew Exploration Vehicle (CEV) and the Crew Launch Vehicle (CLV) are designs that combine elements of the Saturn V vehicle used during the Apollo program with some of the components used in the Space Shuttle. The new vehicle's first stage is an upgrade of the Space Shuttle's Solid Rocket Booster (SRB). The second stage utilizes liquid propellants and uses a LH2/LOX engine that is a derivative of the Saturn rocket's J2 engine. Atop the liquid stage is a service module (SM) and a capsule, which holds the astronauts similar to the Apollo command module. The capsule and the SM together are called the Crew Exploration Vehicle (CEV).

*Computer Scientist, AIAA Senior Member

†Aerospace Engineer

‡Aerospace Engineer

§Aerospace Engineer, AIAA Senior Member

As in the Apollo program, a launch escape system, consisting of an escape rocket motor connected to the capsule, is used in case an abort is deemed necessary due to a failure in the launch system.[1,2] Such an escape system is necessary to meet crew safety requirements of the CEV design. The abort scenario was a topic of study during the Apollo mission due to its importance as the only method of saving the astronauts in case of a disaster. During the design phase, the escape motor was sized based on astronaut safety considerations. An abort test was conducted during the Apollo program and the capsule recontacted the booster shortly after abort initiation.[3] This behavior was due in part to large increases in drag when the bodies are in close proximity. Thus the effects of separation position and other input parameters are important. The primary tools available to the Apollo engineers to study these issues were engineering methods,[4] wind tunnel experiments[5,6] and flight tests.

Since the time of the Apollo program, computer-based simulation capabilities have evolved sufficiently to play a significant role in the design and development of the CLV and in the assessment of the risks involved in the launch and abort processes. In order to use simulation technology for risk evaluation of a specific design, the simulation tools must be validated. The validation of the in-house simulation tools was reported in a previous study.[7] Specifically, the axial and normal forces on the launch escape vehicle were compared to wind tunnel data. During the abort process, the launch escape vehicle is in close proximity of the service module (SM), thus the parameters of interest are position and orientation of the launch escape vehicle with respect to the SM.

This paper has two main objectives. First, two Launch Abort Vehicle (LAV) configurations are studied to determine if an alternative can be found that avoids the heavy drag penalties of the Apollo tractor abort system. The two configurations investigated include a scaled-up Apollo-like Tractor concept, and a Side-Mounted Rockets (SMR) concept. Second, various numerical simulations schemes are examined to determine an accurate and cost-effective way to assess the aerodynamic performance of the LAV.

The primary factor affecting abort performance is the variation of axial force (drag) coefficient with longitudinal separation distance between the LAV and SM, and this is the quantity reported for most of the cases studied in this paper. As a follow-up to the previous validation study, the capabilities of inviscid and viscous computational simulations to accurately predict proximity aerodynamic loads are first assessed against Apollo wind tunnel data. Then steady-state computations are performed at a supersonic freestream Mach number to compare the differences between viscous and inviscid simulations for the current LAV concepts. Next, freestream Mach number effects are studied under thrust-off conditions using inviscid steady-state simulations. Viscous steady-state computations are then utilized to compare thrust/plume-on and thrust/plume-off conditions. The capability of a viscous slow prescribed motion simulation to generate a static database for separation of the LAV from the SM in the axial direction is investigated next. Finally, viscous coupled six-degrees-of-freedom (6-DOF) simulation results for the thrust-on Tractor LAV separation from the SM are compared against viscous static steady-state/prescribed motion data.

II. Configurations

II.A. Tractor Configuration

The geometry of the Tractor concept with the Apollo-like capsule is shown in Fig. 1. At the time this study commenced, no CEV LAV designs were available. A scaled-up Apollo tractor design was used with the capsule diameter scaled to the 5.5 meter dimension considered for the CEV. The mass properties were also scaled accordingly to obtain the required input parameters for 6-DOF simulations.

The LAV consists of the escape motor, the support tower, and the capsule. The motor produces a thrust of 521k lbf to provide a maximum of 15 g's of acceleration at pad abort and supplies 4 nozzles canted 35 degrees from the centerline. The two yaw nozzles output the same amount of thrust, while the top pitch nozzle has a smaller throat than the bottom pitch nozzle. The total thrust vector is directed through the off-axis center of gravity of the vehicle and is intended to pull the vehicle away from the path of the booster. For the wind tunnel validation cases, the entire assembly is mounted on a sting. A second thicker sting surrounds the LAV sting and is used to mount the SM. The SM position was varied along the centerline with displacement from the maximum capsule diameter location denoted by (Δx).

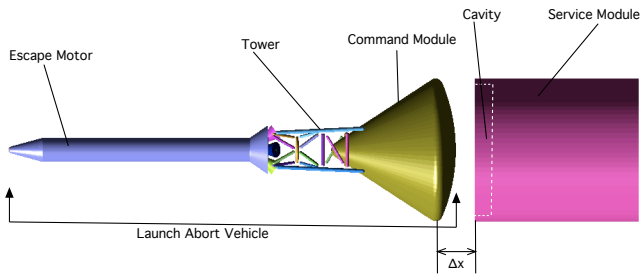

Figure 1. Geometry of the Tractor launch abort vehicle concept.

II.B. Side-Mounted Rockets Configuration

The SMR concept, depicted in Fig. 2, consists of 12 solid rocket motors strapped around the base of the capsule. For simplicity, the attachment structures are not modeled in the simulation. The motors are sized to provide a total of 12 g's acceleration (381k lbf thrust). To avoid the plume impingement drag and provide for the capsule base pressurization, the aft-most point of each of the nozzles is aligned with the axial location of the maximum diameter of the capsule. These nozzles are also canted only 15 degrees from the capsule centerline. The lower cant angle compared to the Tractor configuration minimizes the losses (4% instead of 20%) due to the lateral thrust and helps pressurize the capsule and service module interface to reduce the proximity drag.

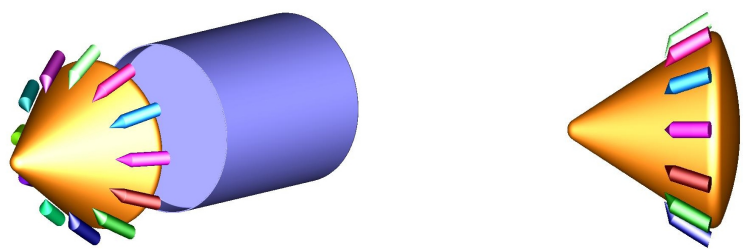

(a) (b)

Figure 2. Geometry of the SMR launch abort vehicle concept. (a) Oblique view of capsule and SM. (b) Side view of capsule and SMR motors.

III. Simulation Methodology

Two computational fluid dynamics (CFD) simulation packages are utilized in the current study to compute solutions of the LAV in the vicinity of the SM. The Cart3D package[8] is used to perform inviscid simulations on unstructured Cartesian meshes while the OVERFLOW-2 package[9] is used for viscous simulations on overset structured meshes. Major steps of the simulation process (geometry definition, mesh generation, flow solution) are described in the following sections. Simulations using static steady-state computations versus relative-motion, dynamic moving-body computations (prescribed motion and coupled 6-DOF) are also discussed.

III.A. Geometry Definition

The geometries of the Tractor components are based on a scaled-up version of the Apollo escape vehicle. These components are defined in several publications from the Apollo program. The tower geometry is discussed in Ref. 6, while the launch escape vehicle is described in detail in Ref. 10. The escape motor nozzle sizes are taken from Ref. 5 and scaled up to match nozzle sizes required for flight conditions. Finally, most other details of the Apollo vehicle geometry are described in Ref. 11. For the current study, the diameter of the capsule (based on the Apollo capsule shape) is scaled up to match the diameter of the CEV

Orion capsule. The geometry for the SMR configuration is constructed using the same capsule and SM as the Tractor configuration. The side-mounted rocket component geometry is mostly conceptual and is not documented in any formal reports or papers.

The geometry definition files for both configurations are constructed using the Chimera Grid Tools software package[12] from analytical descriptions given in blueprints or conceptual drawings. Chimera Grid Tools (CGT) is a collection of software modules written specifically for the efficient generation and manipulation of geometry as well as overset surface and volume meshes. All components of both the Tractor and SMR configurations, including the escape motor, the Tractor support tower with its multiple struts and one ring, the capsule, the service module, and all the rockets of the SMR concept are made using this capability. Furthermore, CGT provides a scripting capability so that the geometry and grid creation can be automated and parameterized, making it simpler to generate the entire grid system for different SM displacements from the LAV.

III.B. Mesh Generation

For the inviscid Cart3D simulations, each component is first created with a structured quadrilateral mesh derived from the CGT-created geometry files. The quadrilateral mesh is then converted to an unstructured surface triangulation. Each component triangulation is carefully made to ensure that the component's wetted surface forms a closed body. These triangulations are then intersected with each other to obtain the final configuration. The result is a triangulation of the vehicle with tagged components. The final triangulation is used to generate an unstructured, telescoping Cartesian field mesh that is coarse in the far-field, but fine close to the surface of the vehicle.[8] The grids for the Tractor and the SMR configuration generated in this manner are shown in Fig. 3 along with the cuts of the Cartesian volume meshes.

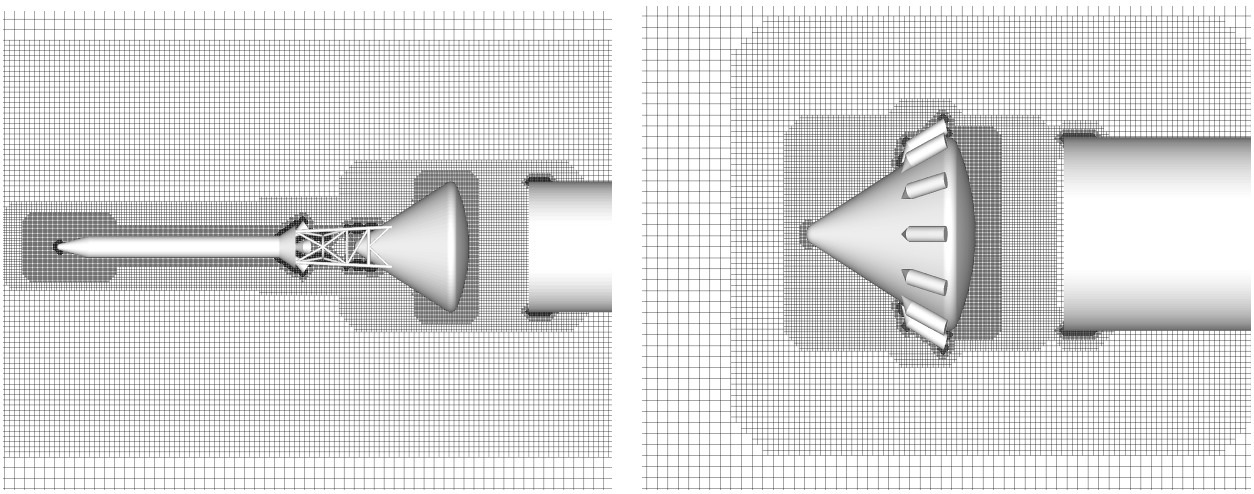

(a) Tractor $\frac{\Delta x}{D} = 0.6$ (b) SMR $\frac{\Delta x}{D} = 0.6$

Figure 3. Cartesian grid systems for Tractor and SMR configurations for Cart3D (inviscid) simulations.

For the viscous overset grid simulations, surface meshes for each component are generated either algebraically or hyperbolically[12] from the CGT-created geometry files. Curvilinear body-fitted near-body volume meshes are then created by marching hyperbolically from the surface meshes. These near-body volume meshes are embedded in telescoping off-body structured Cartesian meshes generated within the OVERFLOW-2 flow solver. Example meshes around the Tractor and SMR LAV geometries are shown in Fig. 4. Typical grid sizes and number of zones for near-body and off-body regions are shown in Table 1. Since the number of grid points and zones changes with separation distances, only nominal and deviation values are given. As can be seen, the numbers can become quite large for the 6-DOF cases which must be run time-accurately.

III.C. Flow Solvers

The Cart3D package[8] used for inviscid simulations is a component-based system that allows triangulations of separate components to be utilized as a starting point for grid generation. Using cut cells at the body

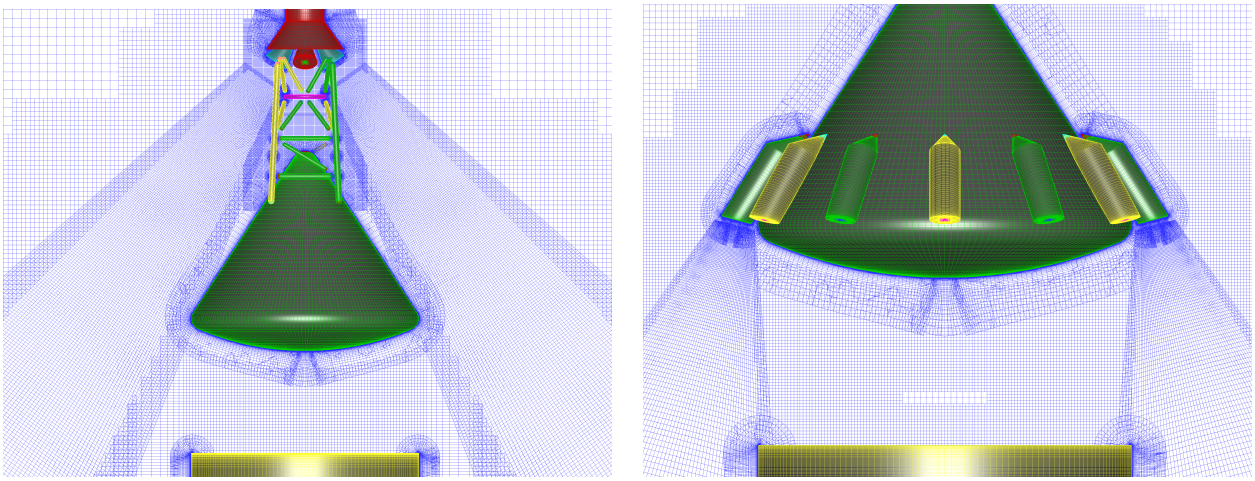

(a) Tractor (b) SMR

Figure 4. Overset grid systems for Tractor and SMR configurations for OVERFLOW (viscous) simulations.

surface, the unstructured Cartesian field grid generation step is essentially automated. The 3-D Euler equations are solved with an upwind scheme that uses Runge-Kutta time integration and multi-grid for convergence acceleration. Under certain conditions such as transonic/subsonic flows or high mesh densities, steady-state solutions are difficult or impossible to achieve. Increasing the numerical dissipation reduces the unsteadiness, but the only direct dissipation control provided is via the limiters. An indirect control is possible by controlling the grid cell size where coarser cell sizes provide more numerical dissipation. In this study, this latter method is not used. The cell sizes are determined by the geometric features rather than the characteristics of the flow field.

The OVERFLOW-2 code[9] used for viscous simulations is a Reynolds averaged Navier-Stokes (RANS) code that utilizes structured overset mesh technology for complex geometry handling and flow solution. Second order accurate central differences with matrix dissipation are employed for the spatial terms. It is found that the full cross-terms of the RANS are required to obtain steady flow as the thin-layer approximation yielded unsteady results. In contrast to the inviscid results, all OVERFLOW-2 predictions yielded steady flow fields if appropriate procedures were followed. The grids are generated following the best practices recommended in Ref. 13. The wall-normal spacing is such that $y^+ < 1$ everywhere and a double fringe zonal overlap is used.

Table 1. Number of Zones and Grid Points for the Viscous Simulations at Flight Reynolds Numbers for each Configuration

Configuration	Number of Grid Points	Number of Zones
Static: Tractor Thrust On/Off	59 ± 2 million	126 near-body 439 ± 10 off-body
Static: SMR Thrust On/Off	62.5 ± 2 million	43 near-body 589 ± 10 off-body
6-DOF: Tractor Thrust On	75 ± 5 million	126 near-body 639 ± 25 off-body

Early on in this study (almost 2 years ago), the Spalart-Allmaras (SA) turbulence model was chosen to perform most of the computations since it was reliable and simple to run. It is anticipated that the model's deficiencies are less influential at small proximity distances between the LAV and SM where flow separation behind the LAV is limited. A comparison of the results obtained using the SA and Baldwin-Barth (BB) models are briefly presented in Section IV.C. A more detailed study of the effects of different turbulence models is beyond the scope of this paper, and is deferred to future investigations.

The inviscid and viscous simulations were performed on the Columbia supercomputer at the NASA Advanced Supercomputing Division at NASA Ames Research Center. A typical inviscid steady-state Cart3D

run with about 16 million grid points utilizing 32 processors converges in about 2 hours of wall clock time (64 CPU hours). A typical viscous steady-state OVERFLOW-2 run with about 60 million grid points utilizing 256 processors converges in about 6 hours of wall clock time (1536 CPU hours). For both inviscid and viscous runs, steady-state convergence is declared when the axial force coefficient on the LAV shows no significant changes with increase in number of time steps, and when the L-2 norm of the flow residuals have dropped 3 to 5 orders of magnitude. Typical convergence histories for the LAV axial force coefficient versus time step number for the viscous computations are shown in Fig. 5. The large number of time steps required for convergence is due to the cavity flow between the base of the LAV capsule and the front cavity of the SM.

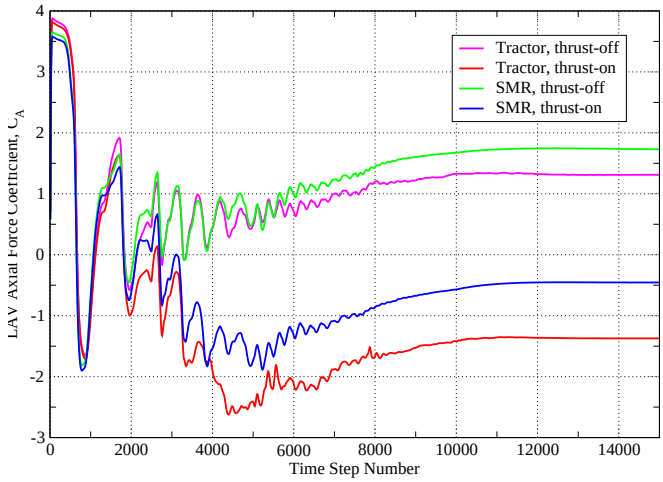

Figure 5. Typical LAV axial force coefficient convergence history for viscous cases.

III.D. Static Steady-State and Prescribed Motion Simulations

Static simulation results are first compared with wind tunnel measurements to validate the simulation process. The proximity effect, namely the variation of the axial force on the LAV with separation distance from the SM, is studied using a series of static steady-state viscous computations at various separation distances.

With a typical viscous static steady-state run taking over 1500 CPU hours to complete on a supercomputer, there is strong motivation to investigate schemes that can speed up the generation of a static database. One method that can potentially offer significant time savings is to perform a prescribed motion simulation to move the LAV at a slow constant speed away from the SM. The simulation begins with the LAV located at a small separation distance $\frac{\Delta x}{D} = 0.039$ from the SM. A static steady-state solution is first computed at this separation distance. Then the computation is continued in time accurate mode until the axial force settles down to a constant value. From here, the prescribed motion simulation begins with a slow start translational velocity which gradually ramps up to the final constant translational velocity.

For this strategy to compare well with static results, the translation speed has to be slow compared to unsteady aerodynamic effects of the motion. If proved applicable, this scheme has two advantages over a series of static runs at various distances. Only a single run is needed for the prescribed motion scheme, and hence a cheaper cost. Moreover, orders of magnitude finer data points for the axial force against separation distance is achieved with the prescribed motion scheme. This is as fine as the number of time steps used for the duration of the simulation. For the computations performed in this study, 15 000 time steps are used to move the LAV a distance of one capsule diameter (or about 0.014 inch per time step). Part of the goal of this study then is to determine if the prescribed motion scheme is a viable method to generate a static database.

III.E. Coupled 6-DOF Simulations

Coupled 6-DOF viscous dynamic simulations are used to obtain accurate trajectories for the Tractor LAV. Although more computationally expensive, a 6-DOF simulation offers better time resolution of the real event over a sequence of static steady-state simulations at varying separation distances. Moreover, unsteady

dynamics effects are automatically included in the 6-DOF computations while these effects are not accounted for in a static database.

The ultimate goal here is to compute the LAV trajectory and flow field during the abort sequence, which is a time-dependent maneuver with the LAV in relative motion to the booster (which is modeled by the SM in the simulations discussed here). Before abort is initiated, the altitude and a representative ascent trajectory are assumed for the LAV-booster vehicle. At the time of abort, the LAV nozzles are switched on and the LAV begins pulling away from the booster. At the same time, it is assumed that the booster engines are shut-down and subsequently the booster continues on its original path and speed. This assumption does not account for deceleration due to drag. However, it is deemed to be adequate for the present simulation due to the much larger inertia of the booster relative to the LAV.

Subsequent to abort initiation, the trajectory of the LAV is computed by a coupled 6-DOF simulation. The mass properties (mass, center of mass, and moments of inertia) of the Tractor configuration are obtained by scaling up from those of the Apollo configuration.[14] The nozzle plumes are modeled in the simulation by specifying appropriate conditions at the nozzle exit planes. The thrust generated by the nozzles is modeled by an applied force in the 6-DOF dynamics computation.

At every time step, the flow solver computes the flow field and the total forces and moments on the LAV, consisting of contributions from aerodynamic, inertial, and applied components. The aerodynamic components are obtained by integrating pressure and viscous stresses on the body surface, while the inertial components are computed from the mass properties of the vehicle. The applied components are prescribed from the designed operational thrust of the nozzles. The flow solver dynamics module returns the new velocities and rotation rates which are used to compute the new position and orientation of the vehicle based on the user supplied time step. The vehicle is then moved that distance, orientation is changed, and the meshes are adjusted for the new position. The time-dependent metrics are computed for the moving-body/moving-grid scenario to preserve the accuracy of the flow-solver. The flow field for the next time step is computed accounting for the new positions and grid speeds. The time-dependent flow field and the trajectory of the vehicle are the results of this time-dependent solution. Time accuracy of the solution is obtained by utilizing 7 steps of dual-time sub-iterations (with one to two orders drop in sub-iterations residuals) per time-accurate time step.

IV. Results

IV.A. Validation of Tractor Configuration Against Wind Tunnel Data

The inviscid and viscous simulation tools used in this paper are first validated against existing experimental data. The original Apollo tractor configuration is used for this purpose since there are extensive Apollo wind tunnel data available for comparison. For this validation, abbreviated results from Ref. 7 are presented to establish a baseline for comparison with the current analyses.

Axial force coefficients (C_A) were measured and reported in an experiment[5] during the Apollo program to establish proximity effects on the escape vehicle during an abort. This experiment used a 0.085 scale model of the Apollo escape vehicle and service module. Presented below are comparisons of the axial force from the simulations and from wind tunnel measurements for several sets of conditions. A range of LAV locations is simulated and their axial forces are compared. As shown in Figure 1, Δx refers to the separation distance between the SM and the capsule along the centerline. The maximum diameter of the capsule D is used as a reference length. The angle of attack is denoted by α per traditional convention.

The axial force results as a function of $\frac{\Delta x}{D}$ are presented in Fig. 6a to show the effect of the plume at various angles of attack. Viscous simulation results are compared to the experiment for nominal thrust and no thrust cases and agree within approximately 5% of the experiment. It can also be seen from these results that the plume is responsible for an increase in drag over the corresponding plume-off cases for a range of angles of attack.

In addition to the plume on/off results, axial forces computed using inviscid simulations are compared to the viscous results and the experiment. These comparisons are shown in Fig. 6b for the no-plume cases at various angles of attack. The figure shows that the inviscid simulations under predicted the drag by about 15% at most angles of attack. In addition, by comparing the axial force coefficient for the LAV at large $\frac{\Delta x}{D}$ values (almost isolated LAV) to the maximum axial force coefficient in near proximity, these results show that the proximity effect is to increase the drag of the isolated LAV by approximately 60%.

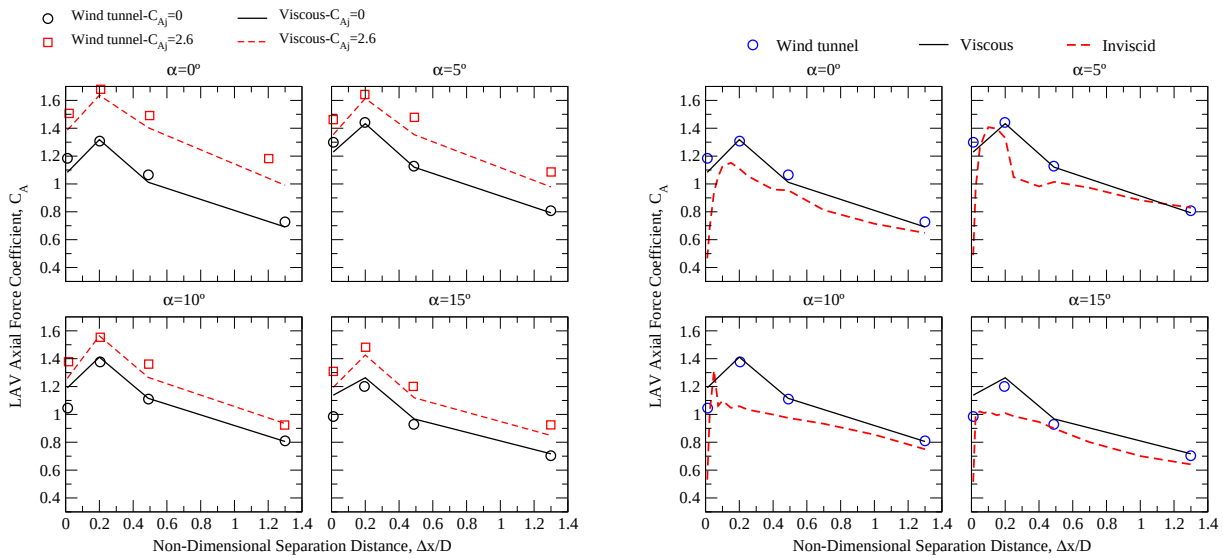

(a) (b)

Figure 6. Axial force coefficient versus $\frac{\Delta x}{D}$ for Tractor wind-tunnel validation runs at $M = 0.9$ and various angles of attack. (a) Comparison of thrust-off and thrust-on results with viscous run. (b) Comparison of inviscid versus viscous results with thrust-off.

IV.B. Steady-State Simulations: Tractor vs. SMR

In this section, comparisons between the Tractor and SMR concepts are presented for a series of static steady-state computations. The differences between inviscid and viscous simulations are first described under thrust-off conditions. Then the effects of freestream Mach number variations are investigated using inviscid computations, also under thrust-off conditions. Finally, the differences between thrust-on and thrust-off conditions are studied using viscous computations.

IV.B.1. Inviscid vs. viscous results

The first steady-state study involves comparing inviscid and viscous results under thrust-off conditions for the Tractor LAV concept. The goal is to establish if the 15% difference in axial force coefficient observed between inviscid and viscous results in the wind tunnel validation runs described in the previous subsection carries over to the current sting-less LAV configurations. For this purpose, steady-state inviscid and prescribed-motion viscous computations are performed at Mach 1.5. It is shown in Section IV.C that the prescribed motion results are essentially the same as those obtained by steady-state computations. A supersonic Mach number is chosen to ensure more reliable results from the inviscid runs. As shown in Fig. 7, the inviscid results produce a lower axial force than the viscous results over the entire range of separation distances. The trends are similar between the inviscid and viscous cases, but the difference varies between 50% at small separation distances and 20% at large separation distances. These results suggest that in situations where trends but not absolute values are needed, inviscid computations may provide a cost-effective way to obtain the results. A few anchor points obtained by viscous computations may help to provide appropriate offsets in generating a database. However, in the presence of large separated flows and cavity flows as are found in these cases, viscous simulations do provide more reliable results than inviscid computations.

IV.B.2. Mach number effects

In this subsection, the variation of axial force with separation distance for a range of Mach numbers (1.1 to 4.0) is studied through a series of inviscid static simulations under thrust-off conditions. Inviscid simulations were used instead of the more expensive viscous simulations for these runs. Since the inviscid simulations were unable to produce consistent convergence at transonic and subsonic Mach numbers, the runs started at Mach 1.1 instead of 0.9. Previous tests from the Apollo program[11] showed that the highest proximity

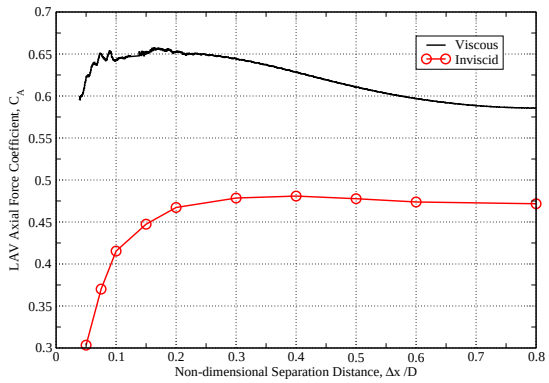

Figure 7. Tractor LAV axial force coefficient against non-dimensional separation distance at Mach 1.5 for viscous prescribed-motion and inviscid steady-state simulations.

drag and minimum-thrust conditions are in the Mach range of 0.7 to 1.1 with 0.9 being the worst case. Furthermore the proximity drag at Mach 1.1 is just slightly less than at Mach 0.9, justifying starting at Mach = 1.1.

The results of the inviscid simulations are shown in Fig. 8. Both the drag and proximity drag effect decrease with increasing Mach numbers. The Mach number trends for the SMR concept are similar to those of the Tractor concept although the absolute levels for the SMR concept are substantially worse with increasing Mach numbers. At Mach 4 the SMR configuration drag is almost 300% higher than the tractor LAV drag. Although the power-on cases were not simulated, it is expected that the base pressurization will not reduce the proximity drag since the proximity drag effects are relatively small for the supersonic flows investigated, i.e. the $15 - 20\%$ effect at Mach 1.1 drops down to essentially 0% at Mach 4.

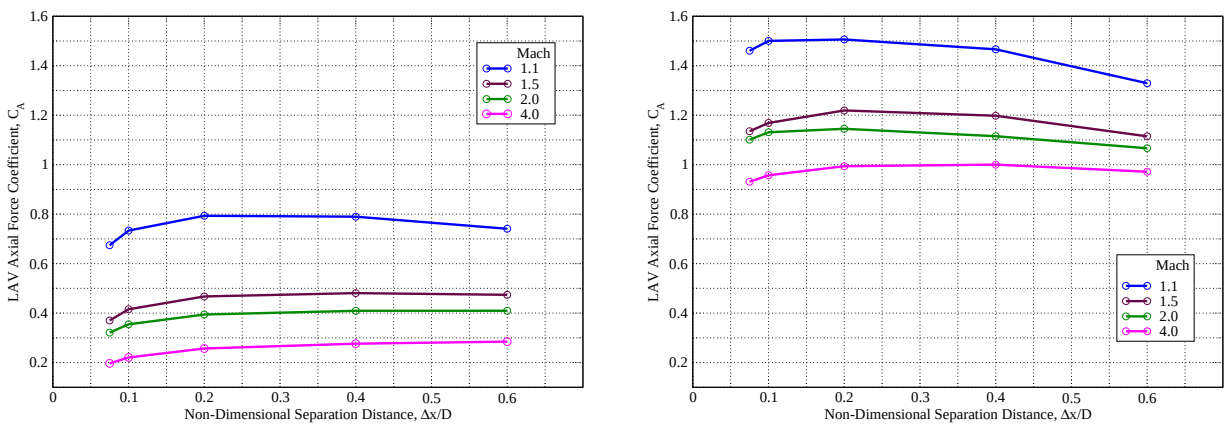

(a) Tractor (b) SMR

Figure 8. Axial force coefficient versus non-dimensional separation distance $\frac{\Delta x}{D}$ at various Mach numbers for inviscid thrust-off simulations.

The pressure on the surface and in the plane of symmetry of the SMR thrust-off configuration at two freestream Mach numbers are shown in Fig. 9. The left hand column shows the pressure for Mach 1.1 and the right column shows the log of the pressure for Mach 4.0. The interesting results represented in this figure are the strong interferences of the SMR motors on the Service Module at small separation distances. This interference vanishes once the separation distances exceed $\frac{\Delta x}{D} = 0.2$. Note also that a log scale is needed to bring out the interference effects on the Service Module at Mach 4. This indicates that the interference effects

on the Service Module are approximately independent of Mach number but the peak pressures increase with Mach number.

IV.B.3. Plume effects

In this subsection, the effects of thrust/plume on and thrust/plume off for the two LAV concepts are studied using viscous computations at Mach 0.9. Figs. 10 and 11 show the surface pressure coefficients and the flow field Mach numbers in the symmetry planes for the SMR and Tractor concepts for both thrust-off and thrust-on cases. The separation distance for this entire set is for $\frac{\Delta x}{D} = 0.6$. As expected, very little plume effect is apparent on the apex part of the capsule for the SMR concept. This is in marked contrast to the Tractor concept where the plumes impinge on the apex side of the capsule. The impinging plumes interact and cause an over-pressure as high as 3.75 psi at Mach 0.9. This over-pressure may be even higher at maximum dynamic pressure (at about Mach 1.63).

Fig. 11b shows that the plume impingement for the tractor concept is substantial. However it does not show the base pressure effect for the SMR concept. The pressurization effect is shown in Fig. 12 where the difference of the capsule surface pressure between the Tractor and SMR LAVs is plotted (ΔP = Tractor pressure - SMR pressure). For visual clarity the tower structure of the Tractor LAV and the escape motors of the SMR LAV are not shown. At a separation distance of $\frac{\Delta x}{D} = 0.075$, the pressure coefficient differential between the two concepts is apparent. Positive values of ΔP (magenta) indicate dominance of the Tractor plume impingement on the capsule on the side view. Negative values of ΔP (green and blue) indicate that the SMR pressure dominates in the base region (base view). The imprint of the 12 SMR motor plumes on the base is also revealed. The SMR surface pressure also dominates on the apex part of the capsule since this is the forward-most part of the LAV for the SMR concept where the pressure is at the stagnation value.

IV.C. Prescribed Motion

In this section, viscous prescribed motion simulations at Mach 0.9 for both LAV concepts under both thrust-off and thrust-on conditions are presented. Fig. 13a shows the LAV axial force coefficient versus $\frac{\Delta x}{D}$ for prescribed motion simulations, and a sequence of static steady-state simulations at various separation distances for four configurations: Tractor thrust-off and thrust-on, SMR thrust-off and thrust-on. The results indicate that the prescribed-motion simulations are able to match the static steady-state results for all the cases and over a good range of $\frac{\Delta x}{D}$. The cost of one prescribed motion run out to $\frac{\Delta x}{D}$ of about 1.0 is approximately equivalent to 20 static steady-state runs. However, a much finer set of data points, about 15 000 over the same range of $\frac{\Delta x}{D}$, is obtained with the prescribed motion computation. One can thus easily conclude that the prescribed motion scheme is a cost effective means to establish a static database (especially in regions of rapid variations at small separation distances).

By comparing the axial force values at the smallest $\frac{\Delta x}{D}$ location, Fig. 13a indicates that under thrust-off conditions and no separation, i.e., under normal operating (no abort) conditions of the vehicle, the Tractor concept has about a 30% lower drag than the SMR concept. If an abort is initiated, the thrust-on curves in the same figure do not show a clear preference between the Tractor and SMR configurations since the drag for one concept is lower than the other, and vice versa at different separation distances. Under thrust-on conditions, the drag for the Tractor concept increases initially before dropping off to its asymptotic value at large separation distances. The proximity effect for the Tractor concept is a difference in drag of about 30% between the maximum value at close proximity to the drag at large separation distances. On the other hand, the thrust-on SMR concept experiences a decrease in drag at the initial separation phase. This decrease in drag is a result of pressurization of the capsule base and SM cavity from the nozzle plumes at small separation distances. Note also that this drop in drag is absent under thrust-off conditions where there is no plume to force the pressurization of the capsule base, nor can it be found in the Tractor configuration where the nozzles are far away from the capsule case and SM cavity.

The maximum proximity drag coefficient experienced for both concepts under thrust-on conditions is about 1.7, which translates to about 292400 lbf of drag. The Tractor weight is about 34733 lbf while the SMR weight is about 31750 lbf. With the Tractor motors thrust at 521000 lbf and the SMR motors thrust at 381000 lbf, the thrust for both concepts is plenty sufficient to overcome both the vehicle weight and aerodynamic drag. Hence, re-contact during the abort maneuver is not likely for either configuration.

Fig. 13b shows a comparison of the LAV axial force variation between the Spalart Allmaras (SA) and the Baldwin Barth (BB) turbulence models. At small separation distances, there is very little difference between

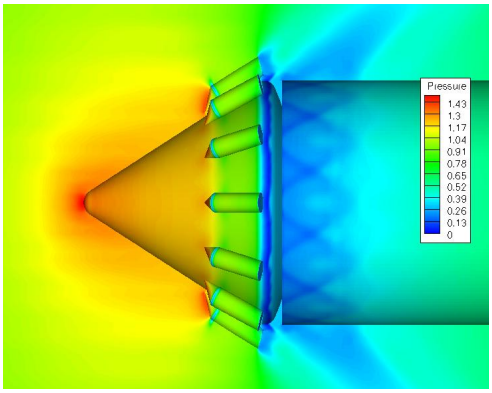

(a) $M = 1.1, \Delta x/D = 0.075$, linear scale

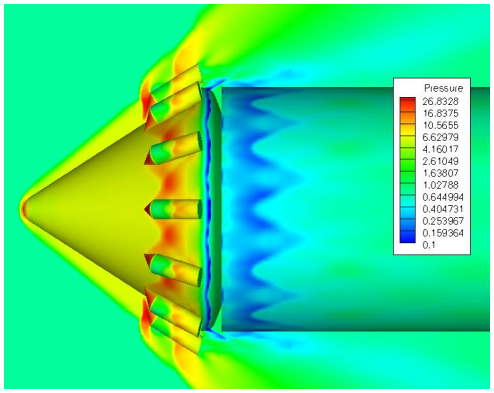

(b) $M = 4.0, \Delta x/D = 0.075$, log scale

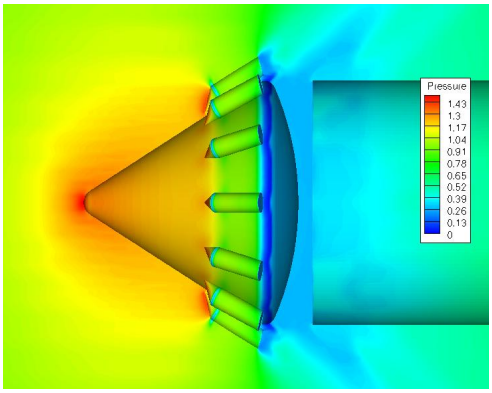

(c) $M = 1.1, \Delta x/D = 0.2$, linear scale

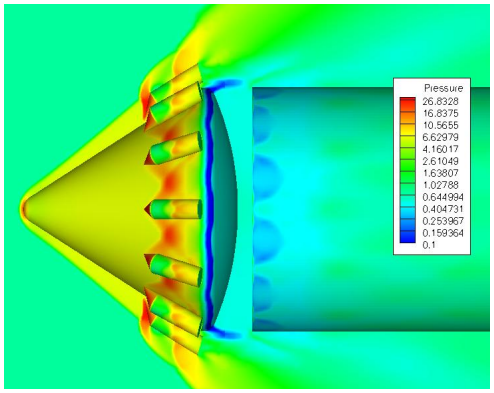

(d) $M = 4.0, \Delta x/D = 0.2$, log scale

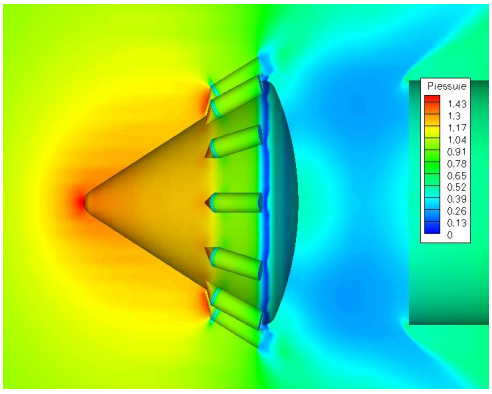

(e) $M = 1.1, \Delta x/D = 0.6$, linear scale

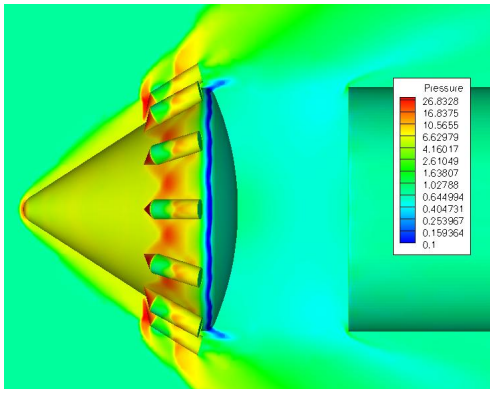

(f) $M = 4.0, \Delta x/D = 0.6$, log scale

Figure 9. Surface and symmetry plane pressure for inviscid simulations on thrust-off SMR configuration.

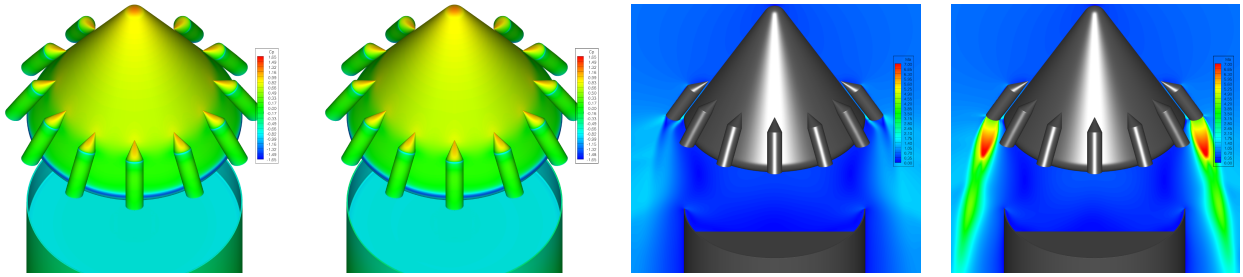

(a) (b) (c) (d)

Figure 10. Steady-state viscous results for SMR concept at $M = 0.9, \Delta x/D = 0.6$, comparing thrust-off versus thrust-on conditions. (a) Surface pressure, thrust-off. (b) Surface pressure, thrust-on. (c) Mach number, thrust-off. (d) Mach number, thrust-on.

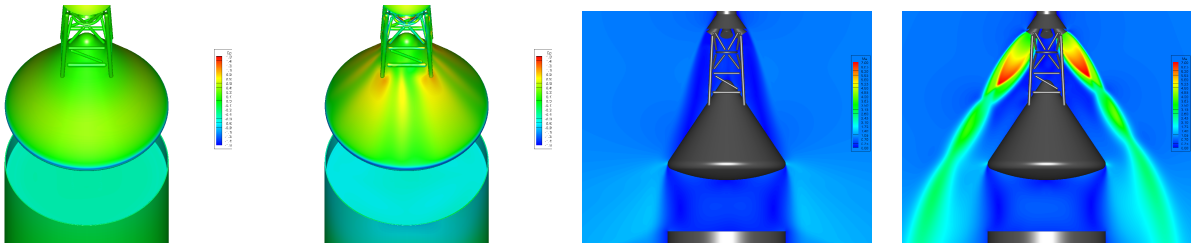

(a) (b) (c) (d)

Figure 11. Steady-state viscous results for Tractor concept at $M = 0.9, \Delta x/D = 0.6$, comparing thrust-off versus thrust-on conditions. (a) Surface pressure, thrust-off. (b) Surface pressure, thrust-on. (c) Mach number, thrust-off. (d) Mach number, thrust-on.

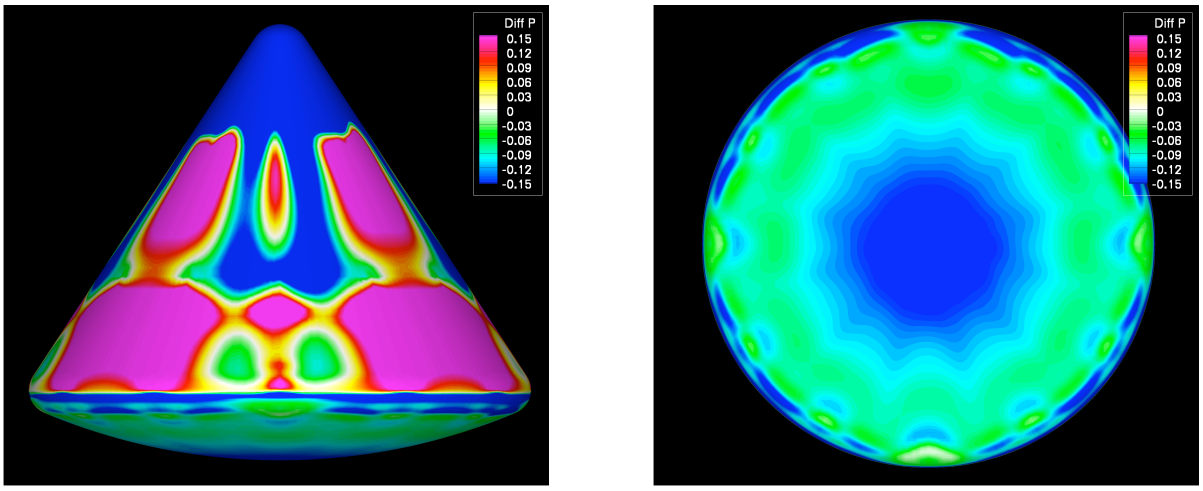

(a) Side view (b) Base view

Figure 12. Surface pressure differential between Tractor and SMR capsule (Tractor pressure - SMR pressure) at thrust-on conditions and $\frac{\Delta x}{D} = 0.075$.

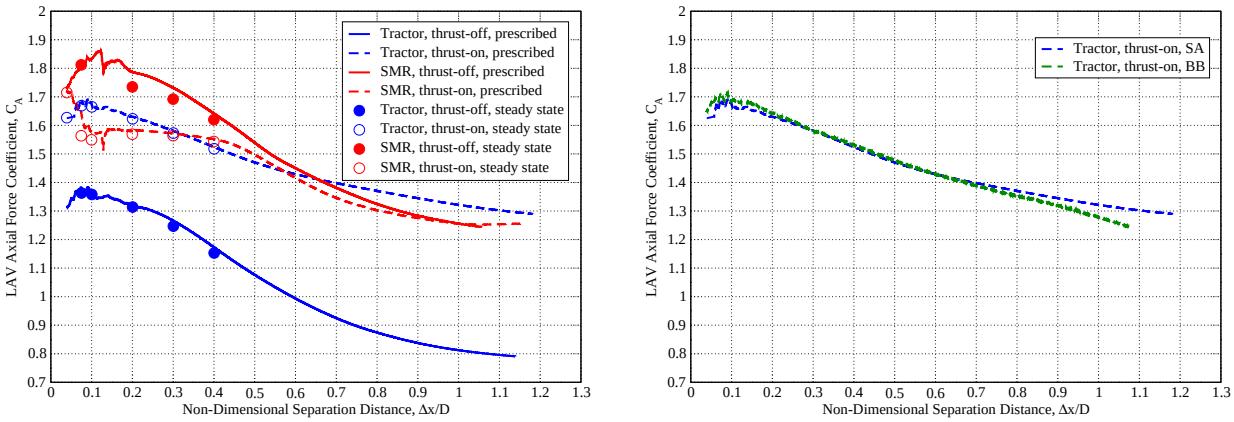

(a) (b)

Figure 13. LAV axial force coefficient against non-dimensional separation distance for viscous simulations at Mach 0.9. (a) Comparison between static steady-state and prescribed motion computations. (b) Comparison between Spalart Allmaras (SA) and Baldwin Barth (BB) turbulence models with prescribed motion.

the two models. As the separation distance increases beyond about $\frac{\Delta x}{D} = 0.7$, the SA model shows a higher drag than the BB model. This is consistent with the anticipated behavior of the SA model which tends to generate higher values of eddy viscosity in the wakes of separated base flows, which in turn tends to increase the drag.

IV.D. Coupled 6-DOF Simulations

Coupled 6-DOF simulations are carried out for LAV aborts at different points in the ascent trajectory for the Tractor configuration. The three abort Mach numbers are 0.9, 1.32, and 2.0, with the corresponding altitudes of 15,874 ft, 30,156 ft, and 48,079 ft, and ambient pressures of 8.3, 4.6, and 2.0 psi, respectively. Three angles of attack (0, 2, and 4 degrees) are also simulated. Partial results of these analyses are shown in Figs. 14–16 as Mach contours in the pitch plane of symmetry and as non-dimensional pressures $\bar{P}/(\gamma\bar{P}_\infty)$ on the surface of the LAV and SM. Each of the figures represents a different abort Mach number and angle of attack with the legends at the same min/max limits so that a direct comparison can be made among all the results.

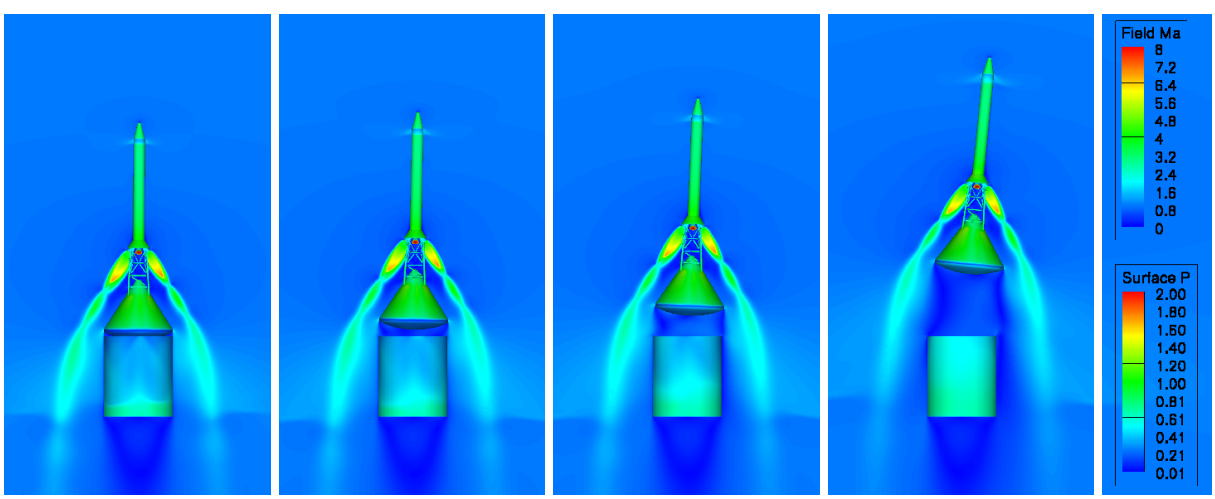

(a) $\Delta x/D = 0.05$ (b) $\Delta x/D = 0.20$ (c) $\Delta x/D = 0.40$ (d) $\Delta x/D = 1.00$

Figure 14. Mach and non-dimensional surface pressure $\bar{P}/(\gamma\bar{P}_\infty)$ contours for Tractor 6-DOF simulation for abort at Mach 0.9, $\alpha = 0$ degree, altitude = 15874 ft., $\bar{P}_\infty = 8.3$ psi. Flow field Mach contours are plotted on the symmetry plane and surface pressure contours are plotted on the LAV and SM surface.

As can be seen in these figures, the plume size and effect increase with increasing abort Mach number and altitude. At Mach 0.9 the plume effect causes an overpressure of about 4 psi on the capsule. At Mach 2.0, the overpressure is still around 4 psi, even though the freestream static pressure has reduced from about 8 psi to 2 psi. This is probably due to the constant nozzle exit pressure. However the plume effect becomes much more important at the higher Mach numbers as can be seen by comparing Figs. 14–16. The separation of the plume from the capsule surface is still quite distinct at Mach 0.9, but at Mach 2.0 and $\alpha = 0$ degree, the plume is grazing the capsule on the windward side of the LAV. This implies that aborts at higher Mach numbers and angles of attack (due to pitch over) need careful consideration.

The axial force coefficients, C_A, as a function of $\frac{\Delta x}{D}$ as obtained from the 6-DOF simulations are plotted in Fig. 17a. The results of the Tractor prescribed motion simulations from Section IV.C are also shown on this plot to provide a comparison between the 6-DOF and prescribed motion results. As shown in the figure, the behavior of C_A obtained from the 6-DOF analyses differs from the prescribed motion simulations.

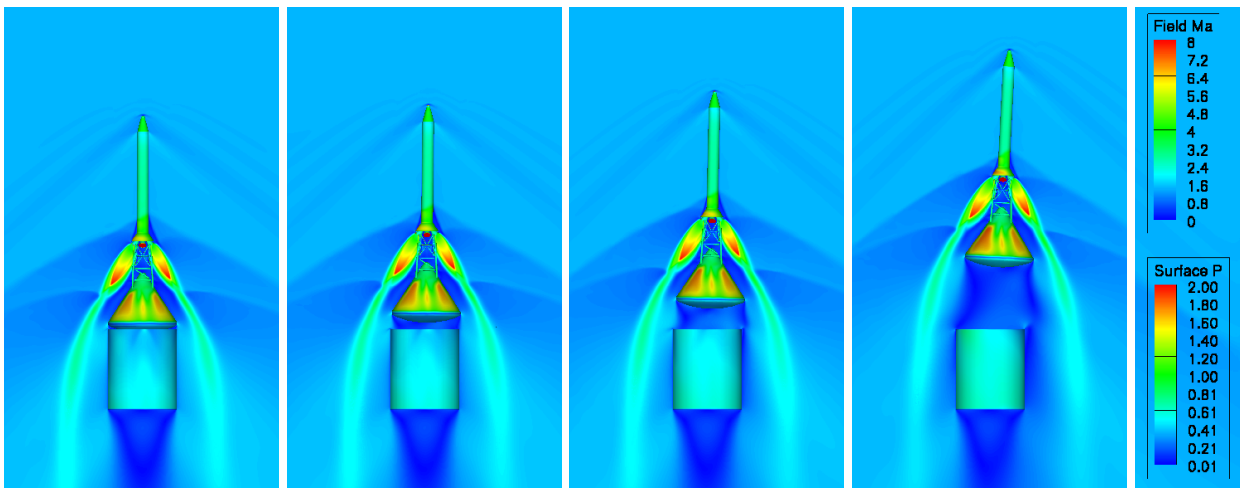

(a) $\Delta x/D = 0.05$ (b) $\Delta x/D = 0.20$ (c) $\Delta x/D = 0.40$ (d) $\Delta x/D = 1.00$

Figure 15. Mach and non-dimensional surface pressure $\bar{P}/(\gamma\bar{P}_\infty)$ contours for Tractor 6-DOF simulation for abort at Mach 1.32, $\alpha = 2.0$ degrees, altitude = 30156 ft., $\bar{P}_\infty = 4.6$ psi. Flow field Mach contours are plotted on the symmetry plane and surface pressure contours are plotted on the LAV and SM surface.

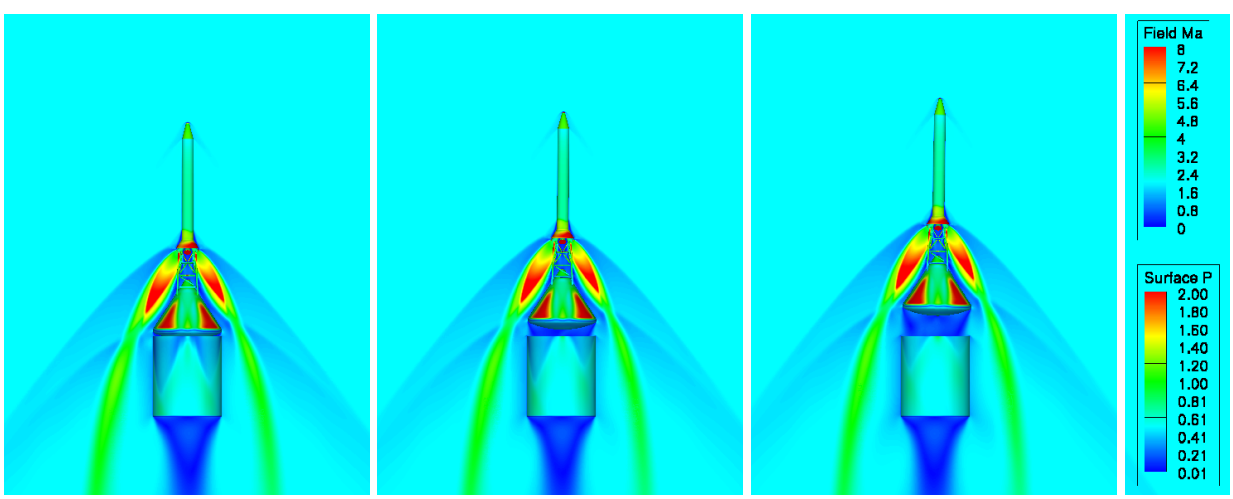

(a) $\Delta x/D = 0.05$ (b) $\Delta x/D = 0.20$ (c) $\Delta x/D = 0.40$

Figure 16. Mach and non-dimensional surface pressure $\bar{P}/(\gamma\bar{P}_\infty)$ contours for Tractor 6-DOF simulation for abort at Mach 2.0, $\alpha = 0$ degree, altitude = 48079 ft., $\bar{P}_\infty = 2.0$ psi. Flow field Mach contours are plotted on the symmetry plane and surface pressure contours are plotted on the LAV and SM surface.

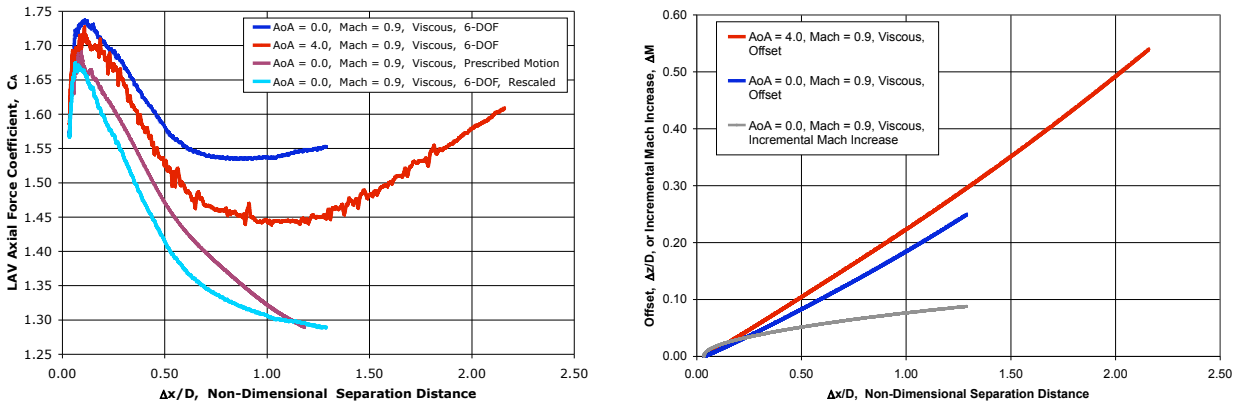

(a) (b)

Figure 17. Viscous 6-DOF simulation results for the Tractor configuration. (a) LAV axial force coefficient against non-dimensional separation distance. (b) Non-dimensional normal offset distance $\Delta z/D$ and Mach number increment ΔM against non-dimensional separation distance.

At small separation distances $\frac{\Delta x}{D}$ of 0.5 and less, the trends and levels are similar. The different C_A characteristics between the 6-DOF and prescribed motion predictions at very small separation distances are due to the different SM lip geometries used in the two types of simulations. The 6-DOF simulations use an SM lip geometry that prevented the capsule and SM from closing tightly without interference between the two components. The prescribed motion analyses of Section IV.C use an SM lip geometry with a beveled edge such that the capsule and SM fitted tightly at $\frac{\Delta x}{D} = 0.0$.

For larger separation distances, the C_A from the dynamic analyses increases and is about 10% larger than that obtained with the prescribed motion analyses. The cause for this behavior is the changing freestream Mach number of the LAV in the 6-DOF simulation as the LAV accelerates away from the SM. This incremental Mach number change (ΔM) due to the acceleration from the 521000 lbf of thrust on the LAV is shown in Fig. 17b. At the initial separation distance, ΔM is zero and increases to almost 0.1 at $\frac{\Delta x}{D} = 1.3$. If the 6-DOF results are re-normalized with the instantaneous Mach number $0.9 + \Delta M$ instead of just 0.9, then we obtain the results shown as the cyan colored curve in Fig. 17a. The differences are now less than 3%.

The remaining differences are due to the changing differential angle of attack and normal offset between the LAV and SM (see Fig. 14). Increases in differential angle of attack and/or normal offset have the effect of pressurizing the cavity between the LAV and SM, and thus decreasing the axial force (drag). At an abort Mach number of 0.9 and an abort angle of attack of 0 degree, the differential angle of attack between the LAV and SM increases to 5 degrees at $\frac{\Delta x}{D} = 1.0$ and about 10-15 degrees at $\frac{\Delta x}{D} = 2.0$. The effect of a larger abort angle of attack (4 degrees) at the same abort Mach number is shown by the red curve in Fig. 17a. Increased pressurization of the cavity reduces the axial force on the LAV. The angle of attack also changes the characteristics of the cavity base flow as shown by the small amplitude high frequency oscillations over the mean value of the axial force, which seems to continue to large separation distances

The change in normal offset distance between the LAV and SM in the 6-DOF simulation is shown in Fig. 17b. As the two components separate longitudinally, they also separate in the normal direction due to the differential thrust level in the pitch plane of the LAV. At a separation distance of one LAV diameter, the offset reached almost 0.2 LAV diameters. This offset also increases the pressurization of the cavity resulting in lower drag on the LAV. In addition, note that the LAV drag approaches the interference free values at smaller separation distances than would be the case for no offsets. Also shown in this figure is the effect of abort angle of attack on the offset. Increasing the abort angle of attack increases the offset (comparing red and blue curves in Fig. 17b).

As was observed in the wind tunnel tests and the static analyses, the proximity drag is at a maximum at an abort Mach number of 0.9 and drops off rapidly with increasing abort Mach number (see Fig. 18). At an abort Mach number of 1.32, the axial drag has dropped almost 30% from that at Mach 0.9. The angle of attack effects on the proximity drag as predicted from the 6-DOF analyses follow the static results. The effects are relatively small for $\frac{\Delta x}{D} < 0.5$ and show a lower drag (about 10%) at $\frac{\Delta x}{D}$ about 1.0 at an abort

Mach number of 0.9. Also, as expected, the axial force increases with separation distance once the LAV accelerates away from the proximity region (because of dynamic pressure increase).

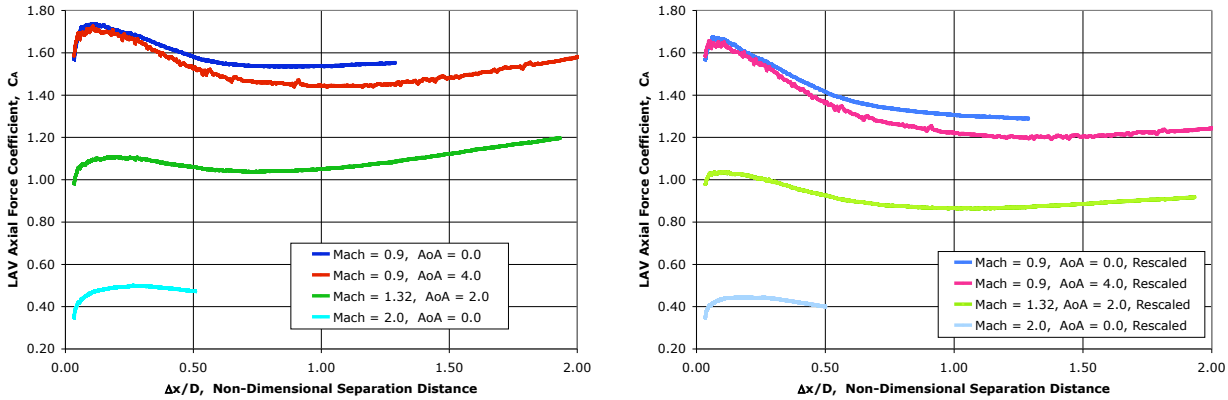

(a) C_A scaled by constant abort conditions

(b) C_A scaled by instantaneous Mach number

Figure 18. Viscous 6-DOF simulations results for Tractor LAV axial force coefficient against non-dimensional separation distance at various abort Mach numbers and angles of attack.

From these 6-DOF simulations it is not clear if the same results could have been generated from static analyses. Further investigation is needed to compare the 6-DOF trajectory with that generated by a trajectory tool based on static data.

V. Concluding Remarks

Two LAV concepts, a scaled up Apollo-like Tractor concept and a conceptual Side Mounted Rockets (SMR) concept, are studied using mostly viscous, and some inviscid simulations. The numerical methods are first validated against Apollo wind tunnel data, where the viscous results are found to agree to within 5%. Although the inviscid simulations were not able to predict absolute levels of the axial force, they did produce similar trends as the viscous simulations.

Since the inviscid simulations are about 10-100 times faster than the viscous simulations, inviscid runs are used to study Mach number trends. It is found that with no thrust/plumes, the Tractor concept experiences a smaller drag than the SMR concept over all Mach numbers from 1.1 to 4.0, and over the entire range of separation distances (from zero to about one capsule diameter) between the LAV and the SM. It is also found that at any separation distance, the drag decreases with increasing Mach number.

The effects of nozzle thrust on and thrust off are investigated using viscous computations at Mach 0.9. Significant plume effects on the capsule are found for the Tractor concept while this effect is absent in the SMR concept due to the aft location of the nozzles. However, the capsule base appears to be more pressurized for the SMR concept than the Tractor concept. Under plume/thrust off conditions (normal operations), the drag for the Tractor concept is about 30% lower than that of the SMR concept. When the plumes are on, neither concept offers a clear advantage over the other over a range of separation distances. For the Tractor concept, there is a drag rise as the LAV pulls away from the SM before the drag decreases with separation distance. For the SMR concept, there is drag reduction due to capsule base pressurization as the LAV pulls away, before the drag levels off and then drops again with increasing separation distance. For both concepts, re-contact is not likely during the abort maneuver since the maximum axial drag experienced plus the weight of the vehicle are well below the axial thrust generated by the respective motors.

The capability of using slow prescribed motion to generate a static database is also studied. It is found that the LAV axial drag agrees with those for static steady-state computations at various separation distances. With the cost of one prescribed motion run (over a separation distance of one capsule diameter) equivalent to about 20 steady-state runs, it is easy to conclude that the prescribed motion simulation is a very cost effective way to obtain a static database (15000 data points in this case).

Coupled 6-DOF viscous computations for several abort Mach numbers are also performed. The results are compared with prescribed motion (static) results. By re-scaling the axial force coefficient to the instantaneous Mach number, the 6-DOF results follow closely to the prescribed motion results for $\frac{\Delta x}{D}$ of about 1 or less.

The slightly lower 6-DOF axial force is caused by pressurization of the LAV-SM cavity from increases in angle of attack and normal offset after abort. Higher abort Mach numbers and angles of attack also have a similar effect of lowering the axial force.

VI. Acknowledgements

Funding for this work was provided by NASA's Simulation Assisted Risk Assessment (SARA) project under the Constellation Program, and the authors would like to thank the members of the SARA team at NASA Ames Research Center for their support.

References

[1]McCarthy, Jr., J. F., Dodds, J. I. and Crowder, R. S., "Development of the Apollo Launch Escape System," *Journal of Spacecraft*, Vol. 5, No. 8, Aug. 1968, pp. 927–932.

[2]Babcock, D. L. and Wiltse, P. D., "Motor-Vehicle Interfaces in the Apollo Launch Escape System," AIAA Paper 65–15, 1965.

[3]Center, M. S., "Post Launch Report for Apollo Mission A-001," NASA TM-X–66755, May 1964.

[4]Boeing, "Saturn V AS-507 Launch Vehicle Operational Abort and Malfunctioned Flight Analysis," NASA CR–130857, July 1969.

[5]Berrier, B. L. and Pendergraft, Jr., O. C., "Transonic Aerodynamic Characteristics of a Powered Wind-Tunnel Model of the Apollo Launch Escape Vehicle During Separation," NASA TM-X–1336, April 1967.

[6]Mosley, Jr., W. C. and Martino, J. C., "Apollo Wind-Tunnel Testing Program Historical Development of General Configurations," NASA TN-D–3748, Dec. 1966.

[7]Pandya, S., Onufer, J., Chan, W., and Klopfer, G., "Capsule Abort Recontact Simulation," AIAA Paper 2006–3324, 2006.

[8]Aftosmis, M. J., Berger, M. J., and Melton, J. E., "Robust and Efficient Cartesian Mesh Generation for Component-Based Geometry," AIAA Paper 97–0196, Jan. 1997.

[9]Buning, P. G., Jespersen, D. C., Pulliam, T. H., Klopfer, G. H., Chan, W. M., Slotnick, J. P., Krist, S. E., and Renze, K. J., "OVERFLOW Users Manual," NASA, 2005.

[10]Mosley, Jr., W. C. and Redd, B., "Aerodynamics Stability Characteristics of the Apollo Launch Escape Vehicle (LEV) with Canard Surfaces Deployed," NASA TN-D–4280, Dec. 1967.

[11]North American Aviation, "Aerodynamics Data Manual for Project Apollo," NASA CR–82907, Jan. 1965.

[12]Chan, W. M., "The OVERGRID Interface for Computational Simulations on Overset Grids," AIAA Paper 2002–3188, 2002.

[13]Chan, W. M., Gomez, R. J., Rogers, S. E., and Buning, P. G., "Best Practices in Overset Grid Generation," AIAA Paper 2002–3191, 2002.

[14]Systems Operations Branch, NASA Johnson Space Center, "CSM/LM Spacecraft Operational Data Book," NASA TM-X–68968, Aug. 1969.